Under consideration for publication in J. Fluids Struct.

Force production and asymmetric deformation of a flexible flapping wing in forward flight

Fang-Bao Tian, Haoxiang Luo[1], Jialei Song
Department of Mechanical Engineering, Vanderbilt University
2301 Vanderbilt Place, Nashville, Tennessee 37235-1592, USA

Xi-Yun Lu
Department of Modern Mechanics, University of Science and Technology of China
Hefei, Anhui 230026, China

Abstract

Insect wings usually are flexible and deform significantly under the combined inertial and aerodynamic load. To study the effect of wing flexibility on both lift and thrust production in forward flight, a two-dimensional numerical simulation is employed to compute the fluid–structure interaction of an elastic wing section translating in an inclined stroke plane while pitching around its leading ledge. The effects of the wing stiffness, mass ratio, stroke plane angle, and flight speed are considered. The results show that the passive pitching due to wing deformation can significantly increase thrust while either maintaining lift at the same level or increasing it simultaneously. Another important finding is that even though the wing structure and actuation kinematics are symmetric, chordwise deformation of the wing shows a larger magnitude during upstroke than during downstroke. The asymmetry is more pronounced when the wing has a low mass ratio so that the fluid-induced deformation is significant. Such an aerodynamic cause may serve as an additional mechanism for the asymmetric deformation pattern observed in real insects.

Keywords: *insect flight, forward flight, fluid–structure interaction, immersed-boundary method.*

1. Introduction

The membranous wings of flying insects usually possess significant structural flexibility and deform considerably during flight (Wootton, 1999; Combes and Daniel, 2003). Such wing elasticity has recently become an important topic of research in the area the flapping-wing aerodynamics. Observations of the kinematics of insect wings have shown that the deformation generally includes both chordwise and spanwise deflections (Ennos, 1988). In many studies, these two types of deformation have been decoupled in the structural representation of the wing so that the model complexity can be reduced and the aerodynamic effect of each type can be investigated separately.

[1]Author for correspondence. E-mail: haoxiang.luo@vanderbilt.edu

Experiments on the wing flexibility have been carried out using heaving-only airfoils or membranous wings in rotational motion (Heathcote et al., 2004, 2008; Mazaheri and Ebrahimi, 2010), and they have demonstrated that both chordwise and spanwise deformations can have positive impact on the thrust performance of the wing. A recent experiment (Ramananarivo et al., 2011) using a mechanical wing self-propelled in air showed that the flapping frequency needs to be significantly lower than the natural frequency of the wing structure in order to achieve maximum thrust and power efficiency.

On the computational side, several models of cruise flight have been developed to simulate the fluid–structure interaction between an elastic wing and its surrounding air. In Zhu (2007) and Michelin and Llewellyn Smith (2009), an oscillatory plate at low angles of attack was used to study thrust production of the wing. Inviscid flow was assumed in their models, and the unsteady wake were accounted for by introducing discrete vortices coming off the trailing edge. Zhang et al. (2010), Spagnolie et al. (2010), and Unger et al. (2012) performed two-dimensional (2D) simulations of the viscous incompressible flow to study the passive pitching of elastically mounted panels or deformable airfoils. Full three-dimensional (3D) studies were also carried out for flexible plunging airfoils to incorporate chordwise and spanwise deformations (e.g., Chimakurthi et al., 2009). In these models, the wing moves in the transverse direction with respect to the flow, and thrust production of the wing is the main focus of the study. In spite of specific wing models being adopted, all these studies have shown that processing some level of structural flexibility may significantly enhance thrust production.

For flapping wings, hovering motion is often used as the flight mode in a study of lift production. If the actuation kinematics of the wing remains the same, then hovering flight can be viewed as the limiting case of forward flight where the freestream velocity (or flight speed) is zero. Using a two-link model representing a chordwise section, Vanella et al. (2009) found that the flexibility can enhance the wing performance by increasing the lift-to-drag and lift-to-power ratios, and that the best performance is obtained when the flapping frequency is near one-third of the natural frequency of the wing structure. With a similar model, Eldredge et al. (2010) investigated the effect of wing flexibility in a range of hovering kinematic parameters. They found that a mildly flexible wing has robust and good performance for a wide range of phase differences between pitching and heaving. Using a dimensionless mass ratio to characterize the relative importance of the inertial force with respect to the aerodynamic force, Yin and Luo (2010) and Dai et al. (2012) performed respectively 2D and 3D simulations to study the performance of a hovering wing at different load combinations. They showed that the dynamic pitching of the wing chord depends largely on the mass ratio and when the aerodynamic torque is comparable to the inertial torque in twisting the wing, the lift efficiency can be further improved significantly.

Insects obviously need both lift and thrust during forward flight. The two force components can be simply achieved by adjusting the angle between the forward direction and the stroke plane, i.e., the plane spanned by wing strokes. However, the details of force production are more complicated than re-orientation of the force vector. The reason is that when the stroke plane angle is less than 90° and the freestream velocity is non-zero, the flow becomes asymmetric between upstroke and downstroke, which leads to the net lift and drag that cannot be calculated through trivial force re-orientation. This argument is illustrated in Fig. 1, where it can be immediately seen that even

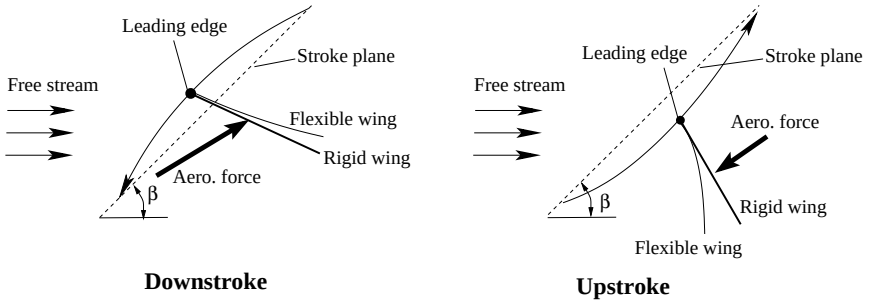

Figure 1: A schematic illustrating the aerodynamic force on a wing chord in a free stream during downstroke and during upstroke, where β is the stroke plane angle.

if the wing kinematics is symmetric in a rotated coordinate system, the resultant aerodynamic force during downstroke would be higher than that during upstroke due to the presence of the free stream.

A direct consequence of the flow asymmetry is that the wing deformation may differ between the two half-strokes if the aerodynamic torque around the torsional axis is large enough to twist the wing. In fact, insect wings typically exhibit significant asymmetric deformation patterns, with the magnitude during upstroke greater than during downstroke (Wootton, 1993). Such a feature is beneficial for the aerodynamics since it reduces the projected wing area and leads to less negative lift during upstroke. Previously, this asymmetry has been mainly attributed to the directional bending stiffness in the wing structure, e.g., one-way hinge (Wootton, 1981), or a pre-existing camber in the wing surface (Wootton, 1993). So far it is still not clear whether the aerodynamic force plays a significant role in this problem. As illustrated in Fig. 1, the aerodynamic force on the wing has a higher magnitude during downstroke. However, instantaneous deformation of the wing chord depends on a combination of the asynchronous aerodynamic and inertial forces, and its asymmetry is therefore not straightforward to predict.

In order to investigate the issues raised here, we propose to study the elastic wing section illustrated in Fig. 1 and consider the stroke plane angle and freestream velocity two variable parameters in addition to the material properties of the wing. While studying lift, thrust, power, and the effect of wing flexibility on these quantities, we will discuss the possible asymmetry in the wing deformation.

2. Problem formulation and numerical approach

We consider a wing section with chord length c as shown in Fig. 2. The velocity of the uniform free stream is U_0. The wing is assumed to be clamped at the leading edge, and the clamping device undergoes a combined translational and rotational motion,

$$\begin{aligned} \mathbf{X}_0(t) &= \frac{A_0}{2}\cos(2\pi f t)[\cos\beta,\ \sin\beta], \\ \alpha(t) &= \frac{\alpha_m}{2}\sin(2\pi f t + \phi), \end{aligned} \tag{1}$$

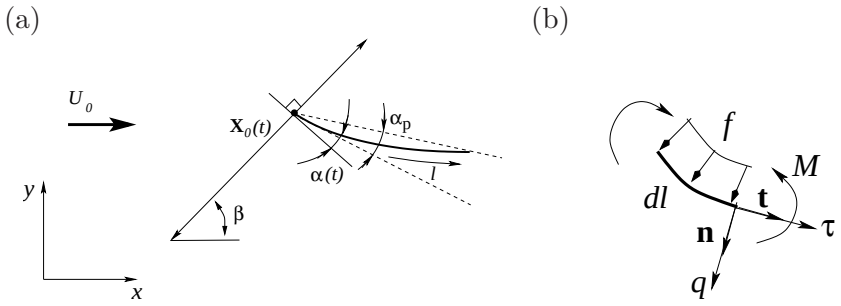

Figure 2: (a) A schematic of the forward flight model, where the wing section translates and pitches in a free stream. The active and passive pitch angles are denoted by α and α_p, respectively. (b) A wing segment illustrating the in-plane tension τ, the transverse stress q, and the bending moment M.

where $\mathbf{X}_0 = [x_0,\ y_0]$ is the position of the leading edge, β is the stroke plane angle, α is the angle between the leading edge and the line perpendicular to the stroke plane, A_0 is the stroke distance of the leading edge, α_m is the amplitude of active pitching, f is the flapping frequency, and ϕ is the phase difference between the rotation and translation. Note that the actuation kinematics as described in Eq. (1) is symmetric between the two half cycles when viewed in the coordinate system rotated by an angle β. Deviation of the leading edge from the stroke plane as illustrated in Fig. 1 has been neglected.

The structural model of the wing is the same as that in Yin and Luo (2010). In this model, the wing is assumed to be elastic and nearly inextensible, and its dynamics is governed by the following nonlinear equation,

$$\rho_s \frac{\mathrm{d}^2\mathbf{X}}{\mathrm{d}t^2} = \frac{\partial}{\partial l}\big(\tau\mathbf{t} + q\mathbf{n}\big) + \mathbf{f}, \tag{2}$$

where ρ_s is the constant linear density of the wing, $\mathbf{X} = [x,\ y]$ is a material point on the wing, l is the arc length from the leading edge, $\mathbf{t} = \frac{\partial \mathbf{x}}{\partial l}$ is the unit tangent vector pointing in the direction of increasing l, $\mathbf{n}$ is the unit normal vector, τ is the tension, q is the transverse stress, and $\mathbf{f}$ is the aerodynamic load distributed on the wing. These internal and external loads on a segment of the wing are shown in Fig. 2(b). The tension is proportional to the tangential strain and is written as

$$\tau = E_S\left(\left|\frac{\partial \mathbf{X}}{\partial l_0}\right| - 1\right), \tag{3}$$

where E_S is the stretching coefficient of the wing and is large for the nearly inextensible wing, and l_0 is the arc length in the unstretched state. The bending moment M in Fig. 2(b) is linearly related to the local curvature κ by $M = E_B\kappa$, where E_B is the bending modulus and $\kappa = -\mathbf{n}\cdot\frac{\partial^2\mathbf{X}}{\partial l^2}$ (this is deduced from $\frac{\partial \mathbf{t}}{\partial l} = -\kappa\mathbf{n}$), and the transverse stress is then given by

$$q = \frac{\partial M}{\partial l} = \frac{\partial(E_B\kappa)}{\partial l} \tag{4}$$

The boundary conditions at $l = 0$, or the leading edge, include the specified position and orientation given by Eq. (1), i.e.,

$$\mathbf{X} = \mathbf{X}_0(t), \qquad \frac{\partial \mathbf{X}}{\partial l} = [\sin(\alpha+\beta),\ -\cos(\alpha+\beta)]. \tag{5}$$

At the trailing edge, $l = c$, both M and q vanish, which requires $\kappa = 0$ and $\partial\kappa/\partial l = 0$. Therefore, we have

$$\frac{\partial^2 \mathbf{X}}{\partial l^2} = 0, \qquad \frac{\partial^3 \mathbf{X}}{\partial l^3} = 0. \tag{6}$$

The flow is governed by the viscous incompressible Navier–Stokes equation and the continuity equation,

$$\begin{aligned} \frac{\partial v_i}{\partial t} + \frac{\partial v_j v_i}{\partial x_j} &= -\frac{1}{\rho_f}\frac{\partial p}{\partial x_i} + \nu_f \frac{\partial^2 v_i}{\partial x_j^2}, \\ \frac{\partial v_i}{\partial x_i} &= 0, \end{aligned} \tag{7}$$

where v_i is the velocity, ρ_f and ν_f are the fluid density and viscosity, and p is the pressure. No-slip and no-penetration conditions are specified at the surface of the wing. To parameterize the problem, we define the non-dimensional groups that include the normalized wing stroke, Reynolds number, velocity ratio, mass ratio, and frequency ratio, given respectively by

$$\frac{A_0}{c}, \quad Re = \frac{Uc}{\nu_f}, \quad U_r = \frac{U_0}{U}, \quad m^* = \frac{\rho_s}{\rho_f c}, \quad \omega^* = \frac{\omega_f}{\omega_n} = \frac{2\pi f}{\omega_n}, \tag{8}$$

where $U = 2fA_0$ is the average translational velocity of the leading edge, $\omega_f = 2\pi f$, and $\omega_n = \frac{k_n^2}{c^2}\sqrt{\frac{E_B}{\rho_s}}$ with $k_n = 1.8751$ is the frequency of the first natural vibration mode of the wing (Landau and Lifshitz, 1986). Physically, m^* represents the ratio between the inertial force of the wing and the aerodynamic pressure, and ω^* represents the wing rigidity.

In the present work, we choose $Re = 100$, $A_0/c = 1.25$, $\alpha_m = \pi/4$, and $\phi = 0$, which corresponds to a symmetrical pitching motion (Wang et al., 2004). The velocity ratio is $U_r = 0.4$ or 0.8. These parameters describing the wing kinematics are selected based on previous work on insect flight (Sun and Wu, 2003; Wang et al., 2004; Maxworthy, 1981). Three mass ratios are considered, $m^* = 1$, 2.5, and 5, which represent the light, medium, and heavy wing, respectively. These values are based on estimate of the surface density of several insect wings (Yin and Luo, 2010; Dai et al., 2012). Although the specific Reynolds numbers for those insects are very different, previous studies (Vanella et al., 2009; Dai et al., 2012) have shown that the effect of wing flexibility is quite consistent for Reynolds numbers up to order of 1000. The frequency ratio ω^* is chosen to vary among 0.0, 0.1, 0.2, ..., 0.8, where $\omega^* = 0.0$ represents a rigid wing and $\omega^* = 0.8$ means that the wing flaps near the natural frequency and is most flexible. It should be noted that the resonant frequency of the system is not exactly the same as the natural frequency of the wing due to the presence of the fluid, and the former frequency could be somewhat slower because of the added-mass effect. Further increasing ω^* to nearly one, i.e., flapping at the natural frequency, would lead to exceedingly large deformation and adverse force production. More discussion regarding this situation can be found in the previous works (Vanella et al., 2009; Yin and Luo, 2010; Ramananarivo et al., 2011).

The equations governing the system, Eq. (2) and (7), are solved numerically in an implicitly coupled manner using an in-house solver. Specifically, the incompressible flow is solved using

a sharp-interface immersed-boundary method with a special treatment to suppress the pressure oscillations associated with the moving boundaries (Luo et al., 2012). In this method, a single-block Cartesian grid is used to discretize the Navier–Stokes equation on a rectangular domain, and a standard central difference scheme is used to discretize all the spatial derivatives. Near the solid surface, the ghost nodes and hybrid nodes are defined to facilitate the interpolation of the flow variables. The Crank–Nicolson scheme is used for the temporal discretization, and a projection-correction approach is used to obtain the pressure and divergence-free velocity field. The infinitely thin membranous wing is augmented with an artificial thickness that is about three times of spacing of the Cartesian grid, and the thickness is automatically reduced as the grid is refined. The wing section is discretized by a set of Lagrangian points distributed uniformly along the wing. A second-order finite-difference scheme is used to calculate the curvature of the wing and to discretize the spatial derivatives in Eq. (2) as well as the associated boundary conditions.

The fluid–structure coupling at each time step is done in an iterative manner. Within each iteration, Eq. (2) and Eq. (7) are solved successively, where the pressure and viscous stresses are updated by the flow solver and are then transferred to the wing as the external load, and the displacement and velocity of the wing are updated by the structural solver and are then used as the boundary conditions for the flow. Furthermore, inner iterations are used within each solver to update the solution variables. To ensure convergence, the pressure load and wing velocity are multiplied by a relaxation factor smaller than one before being transferred between the two solvers. The overall approach is similar to that in Fitzgerald et al. (2011).

The simulation setup is similar to that in Yin and Luo (2010). The computational domain has a size of $25c \times 20c$. We have done extensive tests to make sure that the domain is large enough to achieve satisfactory accuracy of the results. A recent research on hovering flexible wings (Fitzgerald et al., 2011) also used a similar domain size. The entire domain consists of a nonuniform Cartesian grid of 240×272 points. The mesh contains a horizontal band of width $3c$ and a vertical band of width $4c$ in which the grid points are uniformly and densely distributed such that the grid spacing $\Delta x = \Delta y = 0.025c$. A total number of 100 nodes are used to discretize the wing section. The time step size is $\Delta t = 0.0025T$ where T is the period of a flapping cycle. In addition, a grid refinement study has been performed to make sure that the simulation results are grid-independent.

3. Results and discussion

We will first consider two flight speeds, U_r=0.4 and 0.8, and stoke plane angle at $\beta = \pi/4$, and we will discuss in detail lift/thrust production and wing deformation. Once the underlying mechanism of fluid–structure interaction becomes clear, we will then study the effect of the stroke plane angle systematically.

3.1. Effect of wing flexibility on the aerodynamic performance

Fig. 3(a,b) shows the thrust and lift coefficients, $C_T = 2F_T/(\rho_f U^2 c)$ and $C_L = 2F_L/(\rho_f U^2 c)$, averaged over more than twenty flapping cycles for U_r=0.4 and $\beta = \pi/4$. Here F_T and F_L are thrust and lift, respectively. The results are shown for the mass ratio at $m^* = 1$, 2.5, 5 and frequency

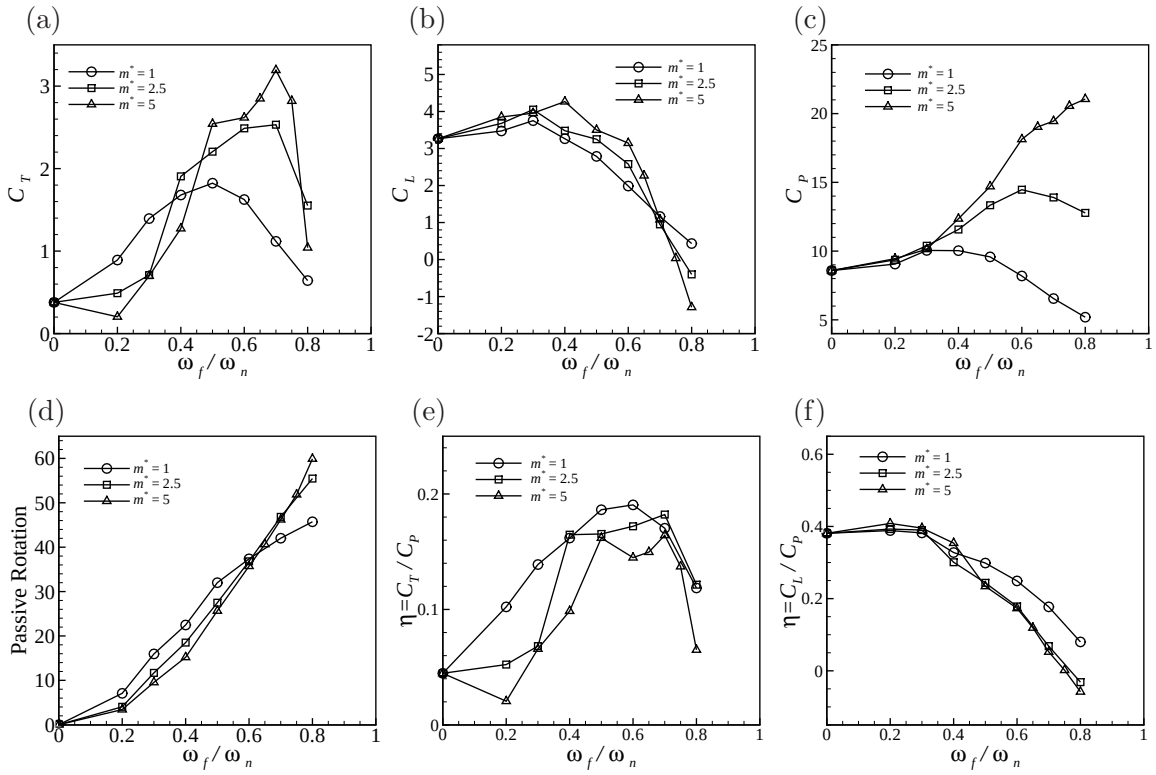

Figure 3: Aerodynamic performance of the wing at $\beta = 45^\circ$ and $U_r = 0.4$. (a) C_T, (b) C_L, (c) C_P, (d) α_p, (e) C_T/C_P, and (f) C_L/C_P.

ratio ω^* from 0 to 0.8. It can be seen that for all mass ratios, wing flexibility has a significant effect on the force production. Specifically, the thrust coefficient peaks at a certain frequency ratio that is between $\omega^* = 0.3$ and $\omega^* = 0.7$, and the peak value is at least three times of that for the rigid wing. For the lift coefficient, the moderate wing flexibility at $\omega^* = 0.3$ to 0.4 leads to a 15% to 30% increase compared to the rigid wing. Therefore, the wing flexibility in the current study could enhance both thrust and lift at the same time. Due to the presence of the free stream, however, the benefits on lift and thrust are not equal even for $\beta = 45^\circ$.

As the wing becomes overly flexible at high frequency ratios, both thrust and lift start to drop sharply, and in particular, the lift coefficient could become negative. Therefore, this result appears to be consistent with the previous study (Ramananarivo et al., 2011) which suggests that flapping at the natural frequency of the wing may not be beneficial for insects from an aerodynamics point of view.

Comparing the three mass ratios, we see that the wing inertia has great influence on the thrust production. Fig. 3(a) shows that at low frequency ratios, $m^* = 1$ has the highest thrust, while at high frequency ratios, $m^* = 5$ leads to the greatest thrust. In addition, as m^* is increased, the peak thrust becomes much higher, and the corresponding optimal ω^* also becomes larger. For $m^* = 1$, the optimal ω^* is around 0.5, and for $m^* = 2.5$ and 5, this optimal value is near $\omega^* = 0.7$. The mass ratio effect on thrust reported here is consistent with that in hovering flight (Yin and Luo, 2010) where $\beta = 0$ and $U_r = 0$. On the other hand, Fig. 3(b) shows that the effect of the mass

ratio on lift is much less significant. All three mass ratios exhibit a similar trend as ω^* is raised.

To analyze power consumption of the wing, we calculate the net aerodynamic power according to $P = -\int_0^L \mathbf{f} \cdot \mathbf{v} \mathrm{d}l$, where $\mathbf{f}$ is the hydrodynamic traction on the wing and $\mathbf{v}$ is the local velocity of the wing. Note that the instantaneous aerodynamic power could be negative since the fluid may do work to the wing temporarily. The power coefficient, C_P, is defined as the aerodynamic power P normalized by $(1/2)\rho_f U^3 c$, and its time-averaged value is plotted in Fig. 3(c). It can be seen that at relatively low flexibility, $\omega^* < 0.3$, the power coefficients for all three mass ratios are very close to each other, and in this region, the flexible wing leads to somewhat higher power requirement than the rigid wing. As the flexibility is further increased to $\omega^* > 0.3$, the power requirement becomes drastically different for the three mass ratios. For $m^* = 5$, the power coefficient rises quickly as ω^* is increased; for $m^* = 2.5$, it first rises and then drops; and for $m^* = 1$, it displays an overall decreasing trend. Thus, for the wings with high flexibility, a high mass ratio leads to significantly greater aerodynamic power requirement than a low mass ratio.

Fig. 3(d) shows the amount of wing deformation as measured by the amplitude of the passive rotation angle, α_p, which is defined as the angle between the undeformed chord and the line connecting the leading and trailing edges (see Fig. 2). The amplitude of this angle is obtained by dividing the difference between the maximum and minimum values of α_p by a factor of 2. As expected, Fig. 3(d) shows that the amount of wing deformation increases as the frequency ratio is raised. At $\omega^* = 0.8$, the nodal displacement of the trailing edge reaches $0.6c$, which justifies the need for the current nonlinear model of the wing. Another observation is that at each frequency ratio, the amount of wing deformation is comparable for the three mass ratios. This feature allows us to focus on the effect of the dynamic wing deformation rather than the magnitude of deformation when comparing different mass ratios.

To show power efficiency of the wing, we present the thrust-to-power ratio, C_T/C_P, and the lift-to-power ratio, C_L/C_P, in Fig. 3(e) and Fig. 3(f), respectively. Overall, the flexible wing may show significantly higher power efficiency compared to the rigid wing. For thrust efficiency, the optimal frequency ratio appears to be around $\omega^* = 0.6$, even though this value is not well defined for $m^* = 2.5$ or 5. The peak thrust efficiency may be four times of the efficiency of the rigid wing. For lift efficiency, the wing flexibility at $\omega^* < 0.3$ also leads to some advantage over the rigid wing, although the power saving is less than 10% and is much less greater than the saving for the thrust. Comparing the mass ratios, we note that $m^* = 1$ in general leads to a greater thrust efficiency than $m^* = 2.5$ and 5 when $\omega^* < 0.7$. However, for lift efficiency, $m^* = 1$ does not have particular advantage over the other two mass ratios unless for high wing flexibility, $\omega^* > 0.5$.

Another series of simulations are performed for a higher flight speed, $U_r = 0.8$, while the stroke plane angle remains at $\beta = 45°$. Thrust, lift, and their efficiency coefficients are plotted in Fig. 4. Compared to the corresponding results in Fig. 3 for $U_r = 0.4$, the thrust coefficient for $U_r = 0.8$ has become significantly lower, while the lift coefficient has increased greatly. Both results are intuitive if the wing is viewed as a fixed airfoil. Another observation from Fig. 4 is that the overall effect of the wing flexibility on thrust/lift production and power efficiency is consistent with what is seen in Fig. 3. Furthermore, the optimal frequency ratios for thrust and thrust efficiency are now between $\omega^* = 0.6$ and 0.7, both becoming higher as U_r is increased. On the other hand, the optimal

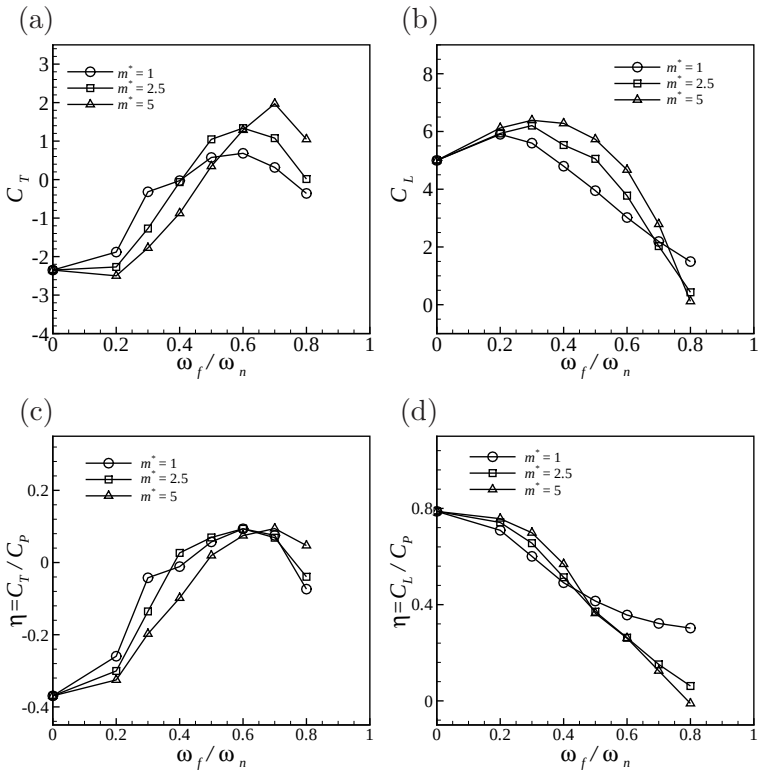

Figure 4: Aerodynamic performance of the wing at $\beta = 45^\circ$ and $U_r = 0.8$. (a) C_T, (b) C_L, (c) C_T/C_P, and (d) C_L/C_P.

frequency ratio for lift is changed only slightly and is now between $\omega^* = 0.2$ and 0.4. Comparing different mass ratios at $U_r = 0.8$, we notice that the lowest mass ratio, $m^* = 1$, does not have clear advantage over the other two mass ratios in terms of power efficiency because this case has a higher thrust-to-power ratio but a lower lift-to-power ratio when ω^* is less than 0.4. This result is different from that in the hovering flight, where a low mass ratio would lead to significantly less power consumption (Yin and Luo, 2010; Dai et al., 2012).

3.2. Instantaneous forces and deformation pattern

To show the relationship between the wing deformation and force production, we need to look into the thrust/lift histories and the instantaneous motion of the wing. For this purpose, we choose two cases where $\beta = 45^\circ$, $U_r = 0.4$, $\omega^* = 0.6$, and $m^* = 1$ or 5. The histories of the thrust, lift, and power coefficients are plotted in Fig. 5, and the corresponding deformation patterns are shown in Fig. 6. The wing displacement in these two cases is fairly large, which makes its effect easy to see.

In Fig. 5, the half cycles representing downstroke has been shaded to better identify the phases of a stroke. As a reference, data for the corresponding rigid wing is also plotted. From Fig. 5(a,b), it can be seen that for both rigid and flexible wings, the downstroke stage in general produces lift, and the upstroke produces thrust, which is expected for insect flight (Wang, 2005). Significant differences can be observed between the flexible and rigid wings and also between the high and low mass ratios. Fig. 5(a) shows that for the rigid wing, most of thrust is produced prior to mid-

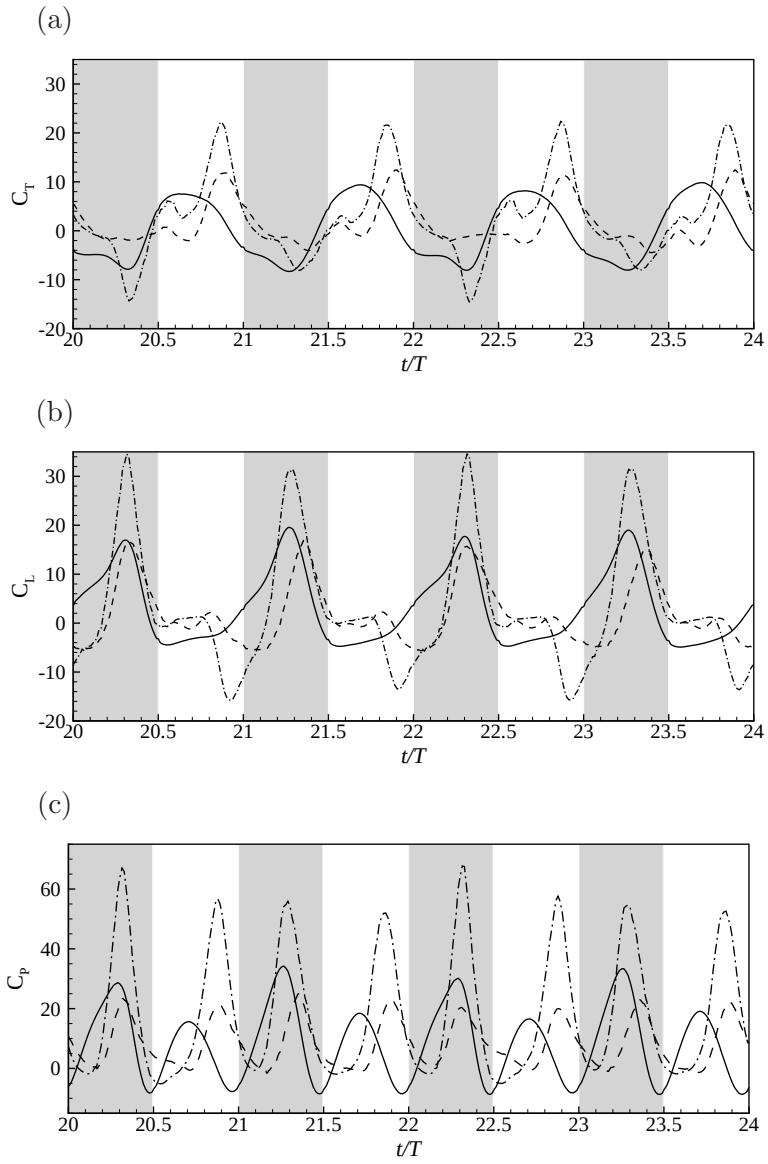

Figure 5: Histories of C_T (a), C_L (b), and C_P (c) for $\beta = 45°$, $U_r = 0.4$, $m^* = 1$ (dashed line) and $m^* = 5$ (dash-dotted line) at $\omega^* = 0.6$, and the rigid wing (solid line). The gray and white regions indicate downstroke and upstroke, respectively.

upstroke, while for the flexible wings, thrust is mainly produced after mid-upstroke and even during the early stage of pronation. Examining the wing deformations shown in Fig. 6(a,b), we observe that during the early stage of upstroke, the flexible wings have a reduced frontal area due to the bending deformation. After mid-upstroke the wings recover from their deformation, and the elastic recoil assists the wings with the thrust production. Another observation is that the wing with high mass ratio, $m^* = 5$, produces the highest peak thrust among the three cases, which is consistent with the averaged thrust in Fig. 3(a). For the low mass ratio, $m^* = 1$, the recoiling motion of the wing is slowed down by the fluid force during the wing deceleration in late upstroke, and thus its thrust has a lower amplitude compared to $m^* = 5$. On the other hand, a significant portion of negative thrust is produced for $m^* = 5$ during downstroke. This force is apparently caused by the

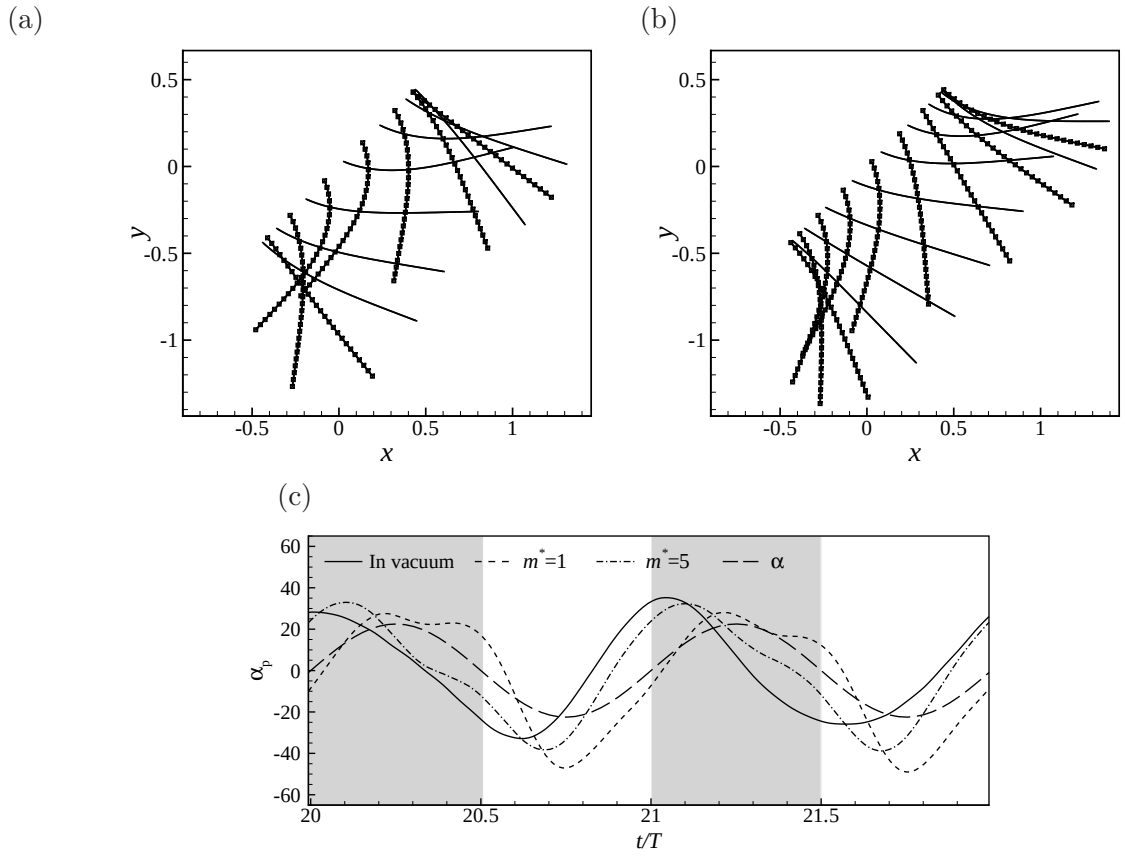

Figure 6: Wing deformation for $\beta = 45^\circ$, $U_r = 0.4$, $\omega^* = 0.6$, $m^* = 1$ (a) and $m^* = 5$ (b). The upstroke frames are marked by symbols. (c) Corresponding passive pitch angle of the wing, where the active pitch angle, α, has been provided as a reference. The gray and white regions indicate downstroke and upstroke, respectively.

inertia-induced wing deformation toward the end of downstroke.

The lift production in Fig. 5(b) shows that peak lift is generated around mid-downstroke for the rigid and $m^* = 5$ cases, but it can be somewhat delayed for $m^* = 1$. Note that cycle-to-cycle variations can be observed for all three cases, and they are more pronounced for the two flexible wings. Like thrust production, the wing with $m^* = 5$ has the highest force oscillations among the three cases, and a significant portion of negative lift is created toward the end of upstroke when wing is pitching upward due to its own inertia. For $m^* = 1$, the negative lift is much less, and it is produced at a later time after the pronation when the wing starts a downstroke. In the present model, the wing forms a reverse camber from pronation to mid-downstroke as seen in Fig. 6(a,b), which is not beneficial lift production. As discussed in Dai et al. (2012), this issue can be alleviated by introducing a pre-existing camber into the model to counteract this downside effect.

Power output here is realized by the wing doing work to the surrounding fluid through the lift and thrust forces. Therefore, both downstroke and upstroke would require a significant portion of power, which is seen from the history of the power coefficient in Fig. 5(c). Comparing the three cases, we notice that the case with $m^* = 5$ has the most power requirement for both downstroke and upstroke and the other two cases have comparable levels of power.

The high power consumption in the case of $m^* = 5$ can be understood from the thrust and lift characteristics of the wing. During downstroke, the wing does work to the fluid through the positive lift and also through the negative thrust after the mid-stroke when the wing, driven the inertia-induced deformation, moves against the free stream. During upstroke, the wing does work through the positive thrust and also through the negative lift, again due to the inertial deformation, near the end of the half-stroke. A similar effect of the mass ratio on power consumption has been discussed for hovering flight previously in Yin and Luo (2010).

Fig. 6(c) shows the instantaneous passive pitch angle, α_p, for $m^* = 1$, 5, and ∞ at $\omega^* = 0.6$. Note that $m^* = \infty$ corresponds to the in-vacuum situation where no fluid force is involved. The active pitch angle, α, is also plotted in the figure as a reference of the phase. It can be seen that there is a consistent phase lag in the passive pitching as the mass ratio is reduced from $m^* = \infty$ to 1. With respect to the active pitch angle, the high-mass-ratio case with $m^* = 5$ shows an advanced effective pitching motion, while the low-mass-ratio case with $m^* = 1$ shows a delayed effective pitching motion. In addition, for $m^* = 1$, the passive pitching during the downstroke is significantly prolonged due to the effect of the fluid-induced deformation. These effects of the mass ratio are consistent with the report in Dai et al. (2012) for hovering flight. As in Dai et al. (2012), the instantaneous pitch angle and pitching rate of the wing are closely related to the thrust/lift characteristics described earlier, and the interaction can be explained by combining the effects of the aerodynamic, inertial, and elastic forces.

An important focus of the present work is the asymmetry in the wing deformation between the two half-strokes. Such an asymmetry can be seen in Fig. 6(c) for $m^* = 1$, where the maximum passive pitch angle is close to 30° during downstroke but is near 48° during upstroke. For $m^* = 5$, the asymmetry is less pronounced, and the reason is that the inertial effect dominating the deformation in this case is symmetric, and the asymmetric aerodynamic effect plays only a minor role.

We further use the cases in Fig. 3 and plot the maximum magnitude of the passive pitch angle during downstroke separately from that during upstroke. The result is shown in Fig. 7(a) for $m^* = 1$ and 5. It can be seen that for all the frequency ratios, the deformation during upstroke is consistently higher than that during downstroke. Furthermore, as the wing becomes more flexible, the asymmetry becomes greater. Beyond $\omega^* = 0.5$, the asymmetry appears to be relatively constant, where for $m^* = 1$, the difference in the passive pitch angle is 15° to 18° between the two half-strokes.

To confirm that the observed asymmetry is due to the presence of the free stream, we have set $U_r = 0$ in the simulation, and the result shows that the deformation pattern becomes mostly symmetric for both $m^* = 1$ and 5. It should be pointed out that a small amount of asymmetry persists even for zero freestream velocity due to the intrinsic behavior of the flow, which has been discussed previously (Godoy Diana et al., 2009). In order to understand the asymmetry shown in Fig. 7(a), we plot in Fig. 7(b) the passive pitch angle along with the torque around the leading edge produced by the aerodynamic force for $\beta = 45°$, $U_r = 0.4$, $m^* = 1$, and $\omega^* = 0.6$. The corresponding wing deformation for this case has been shown in Fig. 6(a). In Fig. 7(b), the aerodynamic torque in both half cycles peaks after mid-stroke when the wing starts to perform the pitching rotation. Furthermore, the magnitude of the downstroke peak is significantly higher than that of the upstroke

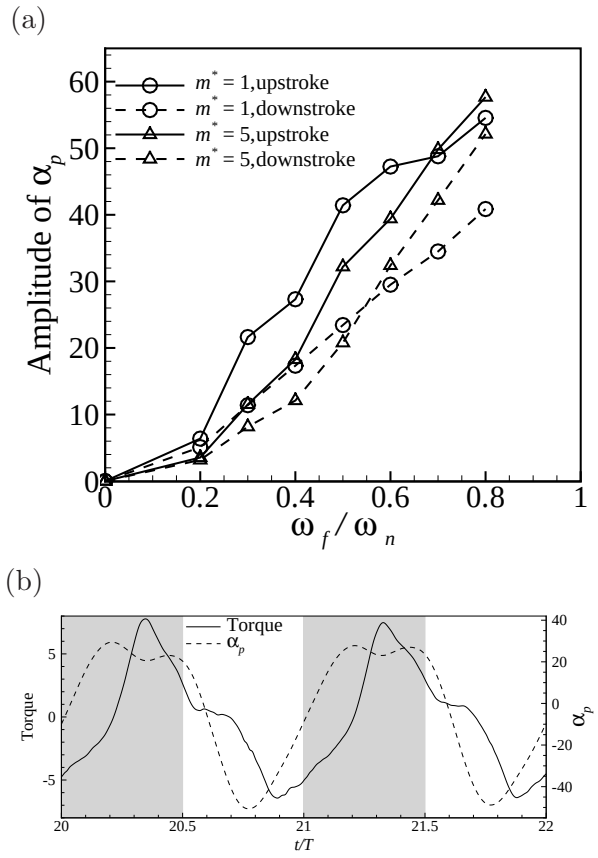

Figure 7: (a) Asymmetric wing deformation for $\beta = 45°$ and $U_r = 0.4$, where the maximum magnitude of the passive pitch angle is shown for both downstroke and upstroke. (b) Aerodynamic torque around the leading edge (left axis) along with the passive pitch angle (right axis) in the case of $m^* = 1$ and $\omega^* = 0.6$.

peak, which is understandable since the wing translates and rotates against the free stream after the mid-downstroke. As a result, the elastic recovery of the wing is delayed prior to supination. This delay is reflected in Fig. 7(b), where the passive pitch angle exhibits a second maximum. After supination, the wing performs upstroke and travels along the free stream at the stroke plane angle. At this moment, the elastic energy is being quickly released. Meanwhile, the leading edge is accelerating for its upstroke. The combined effect leaves the trailing edge much behind the leading edge, and thus the wing forms a greater amount of deformation during upstroke. Therefore, in the present case the asymmetric aerodynamic torque modulates the timing of storage and release of the elastic energy in the wing, which has caused the passive pitch angle in the simulations to be different between the two half-strokes.

3.3. Effect of the stroke plane angle

To systematically investigate the effect of the stroke plane angle, we vary β from 0 to 90° and examine both force production and the wing deformation. Fig. 8 shows the thrust/lift coefficients and also power efficiency for $\omega^* = 0.3$, $U_r = 0.8$, $m^* = 1$ and 5. The rigid wing is included for comparison. In Fig. 8(a), we see that thrust increases monotonically as β is raised, which indicates that the force produced by the wing that is perpendicular to the stroke plane is being

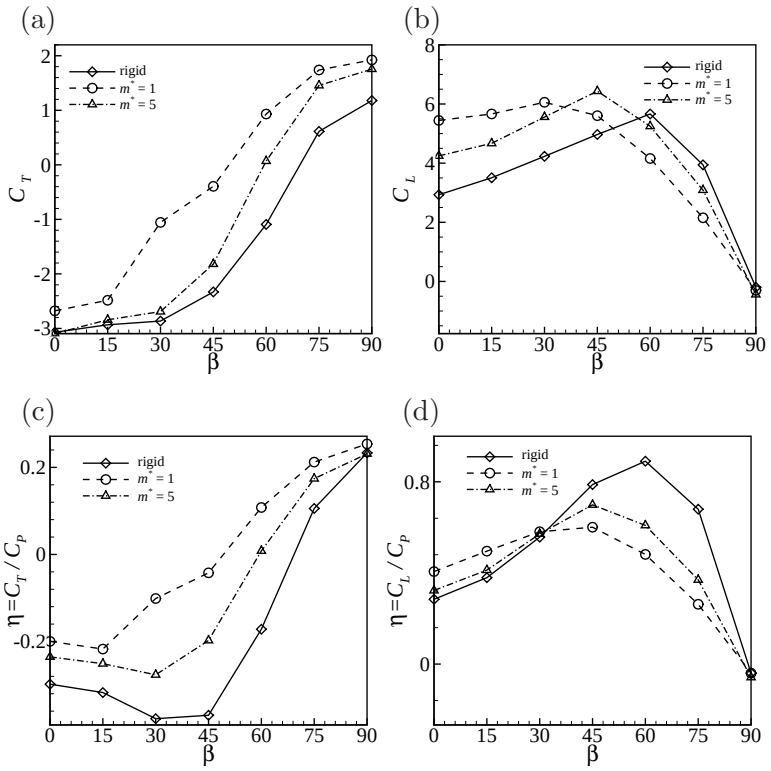

Figure 8: Effect of β on C_T (a), C_L (b), C_T/C_P (c), C_L/C_P (d) for $\omega^* = 0.3$ and $U_r = 0.8$.

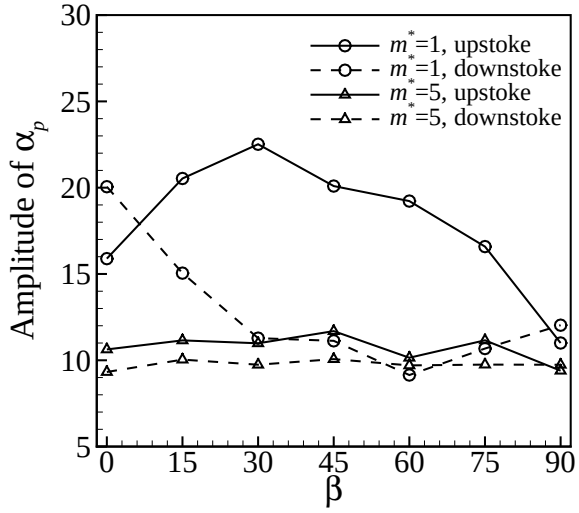

Figure 9: Effect of β on the amount of asymmetric deformation, where the maximum magnitudes of the passive pitch angle during downstroke and upstroke are plotted separately.

directed more horizontally. On the other hand, when β is raised up to a certain degree, the wing during downstroke operates at a favorable angle of attack with respect to the free stream, which is beneficial for lift production. This effect is shown in Fig. 8(b), where C_L generally increases before β reaches 45°.

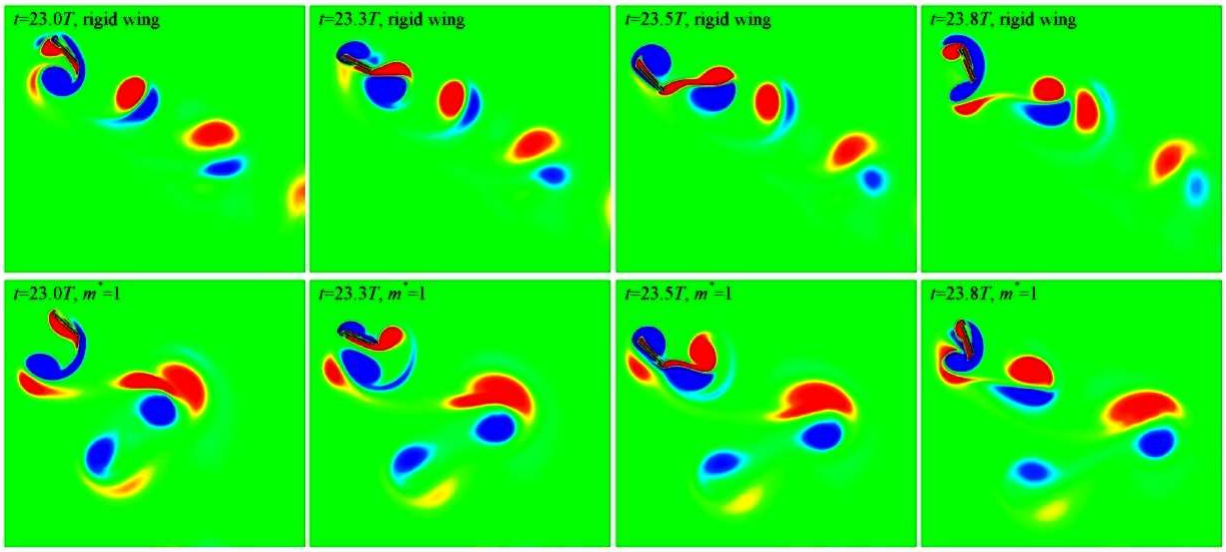

Figure 10: Vorticity contours for a rigid wing (upper row) and a flexible wing with $m^* = 1$ and $\omega^* = 0.3$ (lower row). In both cases, $\beta = 45^\circ$ and $U_r = 0.4$. From left to right, the four frames represent pronation, downstroke, supination, and upstroke, respectively. The contour levels are between $-4U/c$ and $4U/c$.

The efficiency coefficients for thrust and lift exhibit similar trends as for their respective forces. Comparing the three cases shown in Fig. 8, we see that $m^* = 1$ consistently leads to the highest thrust and thrust efficiency, and the rigid case has the lowest thrust. For the lift, the situation is more dependent on the stroke plane angle. For β between 60° and 75°, the rigid case leads to higher lift and a greater lift-to-power ratio than the two flexible cases.

The corresponding asymmetry in the wing deformation is shown in Fig. 9. It can be seen that for most values of β. the wing deformation during upstroke is greater than during downstroke, and the asymmetry is more pronounced for $m^* = 1$ than for $m^* = 5$. At $\beta = 0$, the wing is subject to higher drag when moving against the flow (downstroke) than moving along with the flow (upstroke), so the asymmetry is reversed. We also point out that the wing deformation is not exactly symmetric in the present simulation even when $\beta = 90^\circ$, and a small amount of net lift could be produced, as seen in Fig. 8(b). This non-intuitive result is referred to symmetry breaking of flapping wings and has been studied previously using a rigid foil model that performs symmetrical pitching in a free stream (Godoy Diana et al., 2009).

3.4. Vortical flow structures

Fig. 10 shows the vorticity contours of the flow in a flapping cycle for the rigid case and a flexible case with $m^* = 1$ and $\omega^* = 0.3$. In both cases, $\beta = 45^\circ$ and $U_r = 0.4$. From Fig. 3, thrust is significantly higher in the flexible case, but the lift forces are comparable in the two cases. Overall, the wake consists of a train of vortex pairs shed from the wing. The vortices are convected by the free stream and are meanwhile directed downward, which is consistent with the lift and thrust production of the present wing (Dong et al., 2006). Note that if the free stream is absent, the vortices would be convected roughly in the direction perpendicular to the stroke

plane, as in the previous studies of hovering flight (Eldredge, 2007; Yin and Luo, 2010). In the current case, the free stream has caused significant deflection of the wake. The presence of the free stream also affects formation of the leading-edge vortex by changing the direction of the fluid velocity relative to the wing and reducing the effective angle of attack. Therefore, the leading-edge vortex growth, especially during upstroke, is not as dramatic as that seen in the absence of the free stream. Nevertheless, the main vortex events observed here also appear in hovering flight and have been discussed previously (Vanella et al., 2009; Eldredge et al., 2010), for example, re-encountering of the leading-edge vortex by the wing after reversal, merging of the leading-edge vortex into the wake, and pinching off of the trailing-edge vortex.

Comparing the rigid and the flexible cases in Fig. 10, we notice that the leading-edge vortex is weakened in the flexible case, especially during downstroke. This result can be explained by the reduced angle of attack of the wing due to deformation. In the study of hovering flight by Vanella et al. (2009), the wing flexibility does not have obvious influence on the leading-edge vortex. This discrepancy are likely caused by the choices of the wing model. In Vanella et al. (2009), a two-link model is used, and the leading half of the wing has exactly the same kinematics as the rigid wing. In the current model, the wing deformation is continuous along the chord, which helps to reduce the flow separation near the leading edge. We point out that the translation distance of the wing in the present study is relatively small (here $A_0/c = 1.25$ and is close to that of the dragonfly at the midspan). As a result, the growth of the leading-edge vortex is not as dramatic as that seen in Yin and Luo (2010), where $A_0/c = 2.5$ is used. Nevertheless, the overall effect of the wing flexibility on the leading-edge vortex is similar in these two works. Larger values of A_0/c could lead to detachment of the leading-edge vortex in 2D simulations (Eldredge et al., 2010), but for real insects this vortex could be stabilized by the spanwise flow (Ellington et al., 1996).

Fig. 10 shows that the wing flexibility also has significant influence on the vortices shed from the trailing edge. For example, the vortices are clearly stronger in the flexible case than in the rigid case since the motion of the trailing edge is increased due to the wing deformation. This result is consistent with that in the model of Vanella et al. (2009). Consistent with the force production and the deformation pattern, the vortices in the flow also exhibit an asymmetric behavior between the two half-cycles. For example, the growth of the leading-edge vortex is much suppressed during the downstroke-supination period compared to the upstroke-pronation period. In addition, the positive vortex formed during downstroke is stronger than the negative vortex formed during upstroke. Therefore, the vortex pair of unequal strength in the wake rotate counterclockwise while they are traveling downstream.

4. Conclusions

The two-dimensional fluid–structure interaction of an elastic wing section in the forward flight mode has been computationally investigated in order to understand the effect of wing flexibility on thrust, lift, and power efficiency of the wing. In the model, the leading edge of the wing translates at an angle, i.e., the stroke plane angle, with respect to the free stream, while performing a prescribed pitching motion around itself. The normalized material properties of the wing include the mass ratio and frequency ratio, which represent the wing inertia and bending stiffness, respectively. Note

that although the current model incorporates the chordwise deformation only, the passive pitching caused by the wing bending can still represent pitching of a chord section in a wing with spanwise twist.

By systematically varying the frequency ratio, we found that the dynamic pitching of the wing can greatly increase the thrust and thrust-to-power ratio while maintaining or simultaneously increasing the lift and lift-to-power ratio. In addition, such benefits are relatively consistent for different flight speeds and mass ratios. A high mass ratio leads to greater lift and thrust when the deformation is large, but on the other hand it requires more power input than a low mass ratio due to the negative forces produced by the inertial oscillation of the wing. This result is consistent with the finding in the previous studies by Luo and coworkers for hovering flight (Yin and Luo, 2010; Dai et al., 2012). Furthermore, in the hovering case, a low mass ratio typically leads to better lift efficiency (Yin and Luo, 2010). Due to re-orientation of the stroke plane in the current study, this advantage of the low mass ratio is translated to the thrust efficiency. On the other hand, the current study shows that the low mass ratio does not necessarily have advantage over the high mass ratio for the lift efficiency. The reason is that during downstroke, the fluid-induced deformation at the low mass ratio reduces the effective wing area as well as the lift force.

The optimal frequency ratio of the wing for force production is in general between 0.3 and 0.6 in the present study, which suggests that the flapping frequency should be much lower than the natural frequency for the wing to explore the advantages of the passive deformation. This finding is consistent with the previous numerical studies of hovering flight (Yin and Luo, 2010) and is also supported by a recent experimental study based on a self-propelled wing model (Ramananarivo et al., 2011).

Finally, the presence of the free stream causes significant force asymmetry between downstroke and upstroke since the drag forces produced by the two half-cycles do not cancel each other. Although it is higher during downstroke, the aerodynamic torque modulates the timing and rate of the elastic energy released during supination. Consequently, the wing deformation becomes asymmetric and is greater during upstroke than during downstroke. Such asymmetry persists for a wide range of stroke plane angles and wing rigidity. Consistent with the observed wing deformation pattern of real insects, the result reported in the current study provides a possible additional mechanism for the phenomenon in nature.

Acknowledgments

We would like to acknowledge the grant support from the NSF (No. CBET-0954381), the NNSF of China (No. 10832010), and the Innovation Project of the CAS (No. KJCX2-YW-L05).

References

Chimakurthi, S. K., Tang, J., Palacios, R., Cesnik, C., Shyy, W., 2009. Computational aeroelasticity framework for analyzing flapping wing micro air vehicles. AIAA Journal 47, 1865–1878.

Combes, S. A., Daniel, T. L., 2003. Flexural stiffness in insect wings II. Spatial distribution and dynamic wing bending. Journal of Experimental Biology 206, 2989–2997.

Dai, H., Luo, H., Doyle, J., 2012. Dynamic pitching of an elastic rectangular wing in hovering motion. Journal of Fluid Mechanics 693, 473–499.

Dong, H., Mittal, R., Najjar, F. M., 2006. Wake topology and hydrodynamic performance of low aspect-ratio flapping foils. Journal of Fluid Mechanics 556, 309–343.

Eldredge, J. D., 2007. Numerical simulation of the fluid dynamics of 2d rigid body motion with the vortex particle method. Journal of Computational Physics 221, 626–648.

Eldredge, J. D., Toomey, J., Medina, A., 2010. On the roles of chord-wise flexibility in a flapping wing with hovering kinematics. Journal of Fluid Mechanics 659, 94–115.

Ellington, C. P., Berg, C. V., Willmott, A. P., Thomas, A. L. R., 1996. Leading-dege vortices in insect flight. Nature 384, 626.

Ennos, A. R., 1988. The importance of torsion in the design of insect wings. Journal of Experimental Biology 140, 137–160.

Fitzgerald, T., Valdez, M., Vanella, M., Balaras, E., Balachandran, B., 2011. Flexible flapping systems: computational investigations into fluid–structure interactions. Aeronautical Journal 115, 593–604.

Godoy Diana, R., Marais, C., Aider, J. L., Wesfreid, J. E., 2009. A model for the symmetry breaking of the reverse Bénard-von Kármán vortex street produced by a flapping foil. Journal of Fluid Mechanics 622, 23–32.

Heathcote, S., Martin, D., Gursul, I., 2004. Flexible flapping airfoil propulsion at zero freestream velocity. AIAA Journal 42, 2196–2204.

Heathcote, S., Wang, Z., Gursul, I., 2008. Effect of spanwise flexibility on flapping wing propulsion. Journal of Fluids and Structures 24, 183–199.

Landau, L. D., Lifshitz, E. M., 1986. Theory of Elasticity. Pergamon, New York.

Luo, H., Dai, H., Ferreira de Sousa, P., Yin, B., 2012. On the numerical oscillation of the direct-forcing immersed-boundary method for moving boundaries. Computers & Fluids 56, 61–76.

Maxworthy, T., 1981. The fluid dynamics of insect flight. Annual Review of Fluid Mechanics 13 (1), 329–350.

Mazaheri, K., Ebrahimi, A., 2010. Experimental investigation of the effect of chordwise flexibility on the aerodynamics of flapping wings in hovering flight. Journal of Fluids and Structures 26 (4), 544–558.

Michelin, S., Llewellyn Smith, S. G., 2009. Resonance and propulsion performance of a heaving flexible wing. Physics of Fluids 21, 071902.

Ramananarivo, S., Godoy-Diana, R., Thiria, B., 2011. Rather than resonance, flapping wing flyers may play on aerodynamics to improve performance. Proceedings of the National Academy of Sciences of the United States of America 108, 5964–5969.

Spagnolie, S. E., Moret, L., Shelley, M., Zhang, J., 2010. Surprising behaviors in flapping locomotion with passive pitching. Physics of Fluids 22, 041903.

Sun, M., Wu, J. H., 2003. Aerodynamic force generation and power requirements in forward flight in a fruit fly with modeled wing motion. Journal of Experimental Biology 206, 3065–3083.

Unger, R., Haupt, M., Horst, P., Radespiel, R., 2012. Fluid–structure analysis of a flexible flapping airfoil at low reynolds number flow. Journal of Fluids and Structures 28, 72–88.

Vanella, M., Fitzgerald, T., Preidikman, S., Balaras, E., Balachandran, B., 2009. Influence of flexibility on the aerodynamic performance of a hovering wing. Journal of Experimental Biology 212, 95–105.

Wang, Z. J., 2005. Dissecting insect flight. Annual Review of Fluid Mechanics 37, 183–210.

Wang, Z. J., Birch, J. M., Dickinson, M. H., 2004. Unsteady forces and flows in low Reynolds number hovering flight: two-dimensional computations vs robotic wing experiments. Journal of Experimental Biology 207, 449–460.

Wootton, R., 1981. Support and deformability in insect wings. Journal of Zoology 193 (4), 447–468.

Wootton, R., 1993. Leading edge section and asymmetric twisting in the wings of flying butterflies (insecta, papilionoidea). Journal of Experimental Biology 180 (1), 105.

Wootton, R. J., 1999. Invertebrate paraxial locomotory appendages: Design, deformation and control. Journal of Experimental Biology 202, 3333–3345.

Yin, B., Luo, H., 2010. Effect of wing inertia on hovering performance of flexible flapping wings. Physics of Fluids 22, 111902.

Zhang, J., Liu, N. S., Lu, X. Y., 2010. Locomotion of a passively flapping flat plate. Journal of Fluid Mechanics 659, 43–68.

Zhu, Q., 2007. Numerical simulation of a flapping foil with chordwise or spanwise flexibility. AIAA Journal 45, 2448–2457.